Performance study of the Scintillator Trigger and a Resistive Plate Chamber detector for ANUBIS

CANDIDATE NUMBER: 8234S

SUPERVISOR: Dr Oleg Brandt

MAY 2023

UNIVERSITY OF CAMBRIDGE

ABSTRACT

The ANUBIS experiment proposes installing a set of tracking stations in the ceiling of the ATLAS cavern, in order to look for neutral long-lived particles. These tracking stations are made of layers of Resistive Plate Chamber (RPC) detectors. In this project, we aim to study the performance of one of these RPC singlets, using a trigger setup with two scintillators equipped with Silicon Photomultipliers. The maximum efficiencies of the three scintillators have been determined to be 71.3%, 70.6% and 66.2% at threshold voltages of 660, 680 and 700 mV respectively, using a separation of 20 cm between the top and bottom scintillators. At larger separations, the efficiency is lower. The bias voltage applied to the SiPMs has been optimized to 32 V. We have also tested the front-end boards that read out signals from the RPC strips using a low voltage system and connected them to the data acquisition system.

Acknowledgements

I would like to thank all the members in the ANUBIS group who have always been eager to help.

A big thank you to my supervisor, Prof. Oleg Brandt, for his guidance throughout this project. Thank you for always pushing us to go further with our investigations and to fully understand our results. And thank you for supporting me when I came across any difficulties by making such helpful suggestions.

Thank you to Richard Shaw and Stephen Wotton for their invaluable help with the building of the setups and for helping us resolve any issues that came across.

A very special thank you to my project partner, Jindrich Jelinek, for his kind help to introduce me to the hardware part of the project and for his generosity in sharing his results.

Thank you also to my director of studies and to my family and friends, who motivated me throughout the process.

Table of contents

1. Introduction

The Standard Model (SM) is an elegant mathematical theory that describes the fundamental particles and interactions of our universe. Although it has demonstrated huge successes in providing experimental predictions it fails to explain some phenomena: the existence of dark matter, the baryon asymmetry of the Universe, neutrino masses and the gauge hierarchy problem. To address these inadequacies, many Beyond the Standard Model (BSM) theories have been developed: Supersymmetric (SUSY) models, Neutral Naturalness, Dark Matter models and Effective Portals to Hidden Sectors. These theories predict particles with very long lifetimes, called long-lived particles (LLPs). Many experiments at the Large Hadron Collider (LHC) have looked for neutral LLPs which could be produced in pp collisions, but no direct evidence has yet been observed.

The absence of experimental evidence could be due to a lack of experimental sensitivity. Neutral LLPs with lifetimes larger than the maximum range of the detectors can go through undetected. New detector proposals are aiming to improve the sensitivity of the LHC experiments. The projects MATHUSLA [1] and CODEX-b [2] propose installing a set of detectors in a surface of the CMS and in a region of the LHCb cavern, respectively. The ANUBIS [3] proposal offers a detector structure which consists of several layers of Resistive Plate Chamber (RPC) detectors affixed at the ceiling of the ATLAS experiment's cavern (figure 1), in this way maintaining competitive installation and operation costs. Figure 2 shows how ANUBIS surpasses the standard CODEX-b scenario in the entire relevant phase space, outperforms MATHUSLA for LLPs with $c\tau \gtrsim 10$ m, and extends the reach of ATLAS by many orders of magnitude at $c\tau \gtrsim 1$ m.

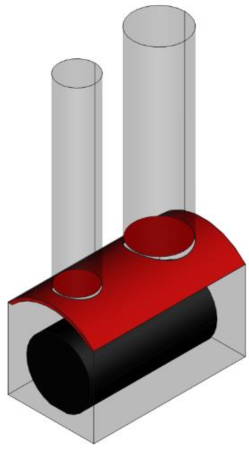

Figure 1. Schematics showing the proposed layout for the ANUBIS project. The ATLAS Experiment is shown as a black cylinder with ANUBIS RPC detectors shown in red [4].

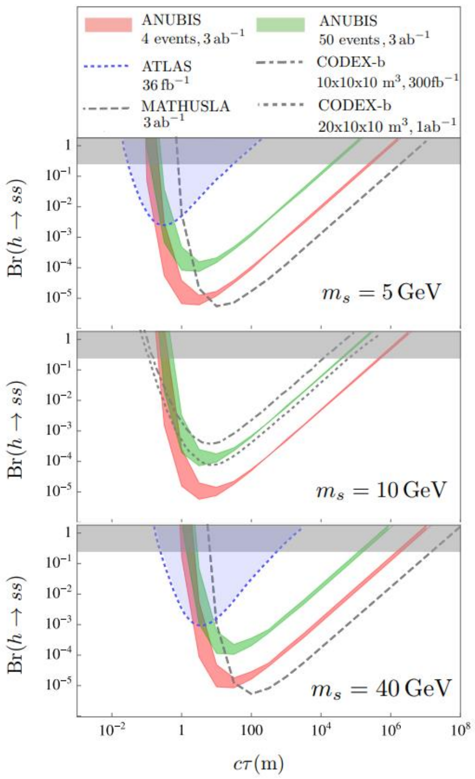

Figure 2. Projected sensitivity of ANUBIS, CODEX-b, and MATHUSLA for LLPs for Higgs decays h→ss with different LLP masses m_s , at the HL-LHC with $\sqrt{s}$=14 TeV. The impact of extending the ANUBIS decay volume up to the ATLAS muon spectrometer is indicated by the filled area. The gray parameter space is excluded by the existing constraints on invisible Higgs decays. The region excluded by a dedicated Higgs portal LLP search with ATLAS is shown for comparison [3].

ANUBIS considers LLPs being produced by a Higgs portal BSM mechanism. The dominant process is gluon fusion (ggF), shown in figure 3. We expect the LLPs to have a Higgs-like Yukawa coupling, making the decay into a pair of $b\bar{b}$ very likely. The quarks hadronise, giving a jet of charged particles that are observable by ANUBIS detector systems. These jets can then be reconstructed back to the vertex to determine the position where the LLP decayed.

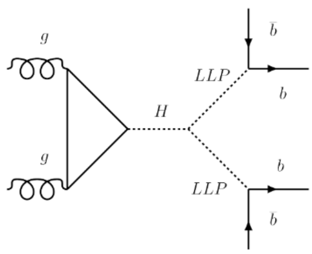

Figure 3. Feynman diagram for ggF producing a Higgs boson H [3].

The proANUBIS prototype has been constructed to achieve the following goals: provide a proof of principle for the hardware, reconstruct cosmic ray events, and validate the background rates predicted from simulation. It imitates one cell of an ANUBIS tracking station by consisting of six BIS7S RPC singlets measuring 180 × 100 cm^2. It has recently been installed in the ATLAS experimental cavern, with commissioning expected in the following months. There will be another proANUBIS prototype used for general performance studies and radiation hardness using eco gases.

In this project we aim to study the performance of one of the RPC singlets that are used for proANUBIS, using cosmic muons. We will use a trigger setup with two scintillator detectors equipped with Silicon Photomultipliers (SiPMs), for which we need to determine the efficiency. The first part of the project consists in investigating the voltages and configurations that result in a maximum efficiency of the scintillator trigger. This part was done in collaboration with Jindrich Jelinek, also a part III physics student at the University of Cambridge. The second part consists in testing the front-end boards of the RPC using a low voltage system.

Section 2 describes the detectors and the experimental setup used. The efficiency measurements of the scintillators are given in section 3 and the work done on the RPC front-end boards is explained in section 4. The conclusions of this project are given in section 6, along with some suggested future studies.

2. Detectors and experimental setup

2.1. Resistive Plate Chamber (RPC) detectors

A Resistive Plate Chamber (RPC) is a type of detector widely used in high energy physics, generally to detect muons. It consists of two high resistivity electrode plates separated by a high voltage and filled with some ionising gas. The ionisation of a charged particle travelling through the gas gap creates electron-ion pairs, where electrons drift and multiply into a Townsend avalanche.

The read-out signal is not made of the avalanche electrons but is induced by the movement of the charges in the gas gap on detection strips. As the electrodes are made of a resistive material, the drop in the electric field is contained locally in the position of ionisation and keeps the rest of the volume sensitive to the passage of other charged particles.

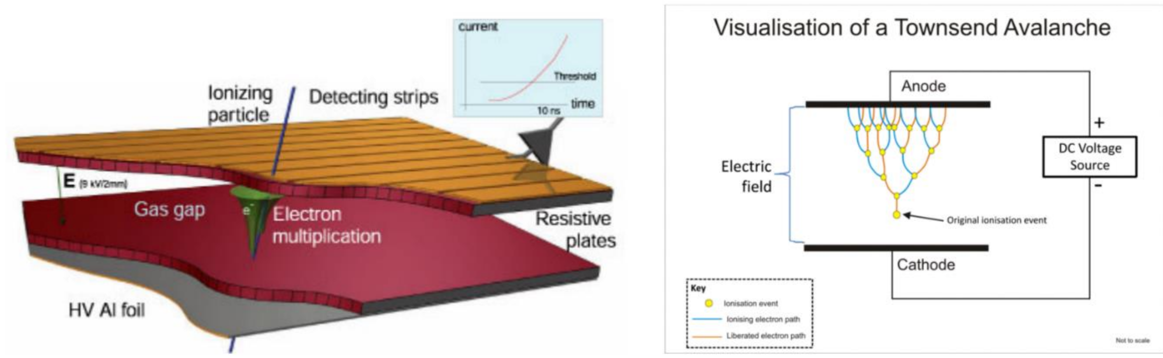

(a) (b)

Figure 4. (a) Principle of operation of RPC. (b) Schematic development of a Townsend avalanche [5].

The mean integrated energy loss through excitation and ionisation processes is given by the Bethe formula. Figure 5 shows the mean integrated energy loss as a function of momentum for a muon in different mediums.

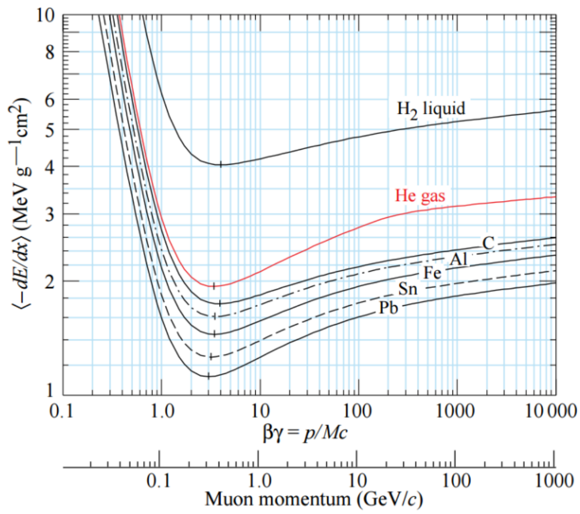

Figure 5. Mean integrated energy loss as a function of muon momentum for different mediums [5].

In this project we aim to measure the efficiency of a BIS7S RPC singlet, composed of two 25 mm pitch strip panels measuring 180 x 100 cm^2 separated by a 1 mm gas gap. One strip panel has 64 strips running in the eta (100 cm long) dimension with 8 front-end boards (FEBs) soldered to the ends of the strips in one side, in order to read out signal, and termination resistors soldered to the other end of the strips, in order to match impedance and eliminate signal reflection. The second strip panel has 32 strips running in the phi (180 cm long) dimension, with 4 FEBs and the termination resistors.

Figure 6. Picture of the BIS7S RPC board in the laboratory at Cambridge. The eta side is facing the camera.

2.2. Scintillator detectors and Silicon Photomultipliers

A scintillator is a material that luminesces when excited by ionising radiation. In this experiment we use EJ-200 scintillators [6] of size 50 x 50 cm^2, covered in a black plastic wrapping to isolate them from external light. The photon emission spectrum of the EJ-200 scintillator peaks at a wavelength of 425 nm, as shown on figure 7. It is important that this wavelength is matched to the wavelength at which the sensitivity of the SiPMs is maximised.

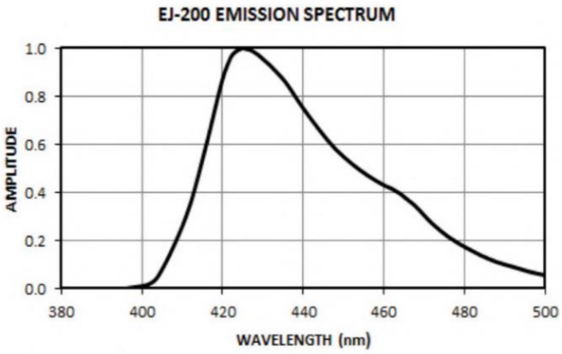

Figure 7. The photon emission spectrum of an EJ-200 scintillator as a function of wavelength [6].

Silicon photomultipliers (SiPMs) are arrays of single photon avalanche diodes (SPADs) operated in Geiger mode designed to detect extremely weak light, down to the single photon. The photons emitted by ionisation in the scintillators hit the SiPMs and create electron-hole pairs, which are then converted into an output signal with a very high gain. There is a breakdown voltage that corresponds to the minimum electric field to give the produced electron-hole pair enough kinetic energy to create further pairs, until an avalanche is produced.

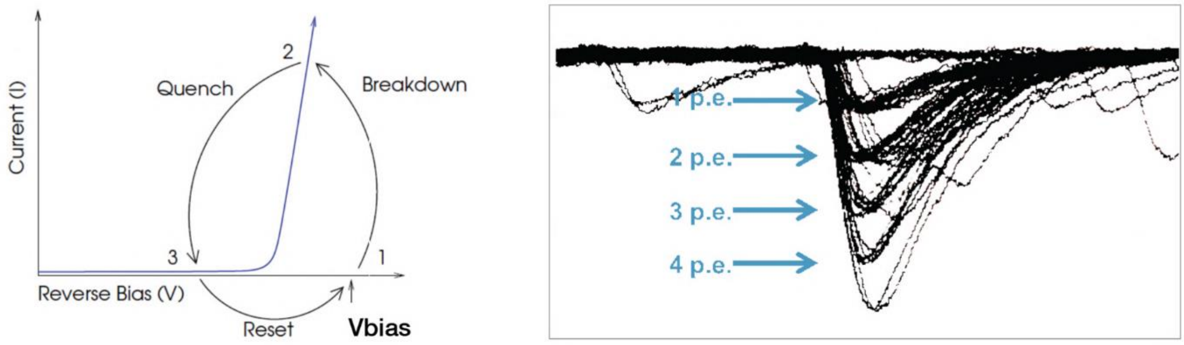

a) b)

Figure 8. a) Breakdown, quench and reset cycle of a SPAD working in Geiger mode. b) Oscilloscope shot showing the discrete nature of the SiPM output when illuminated by brief pulses of low-level light, the amplitude of the signal is proportional to the number of photons hitting the sensor [7].

The two main factors affecting the efficiency of SiPMs are the dark count rate (DCR) and the photon detection efficiency (PDE). The DCR refers to the thermally generated electrons which create avalanches in the same way that a photon would. It is the main source of noise. The PDE is a measure of the sensitivity of the SiPM as a function of wavelength.

There are two types of SiPMs used in this project: Ketek PM3315-WB-B0 [8] and Broadcom AFBR-S4N33C013 [9]. They are both chosen for their high PDE and a low DCR noise. The PDEs for both Broadcom and Ketek, shown in figure 9, have the peak at a wavelength around 425nm, which matches that of the scintillator’s emission spectrum.

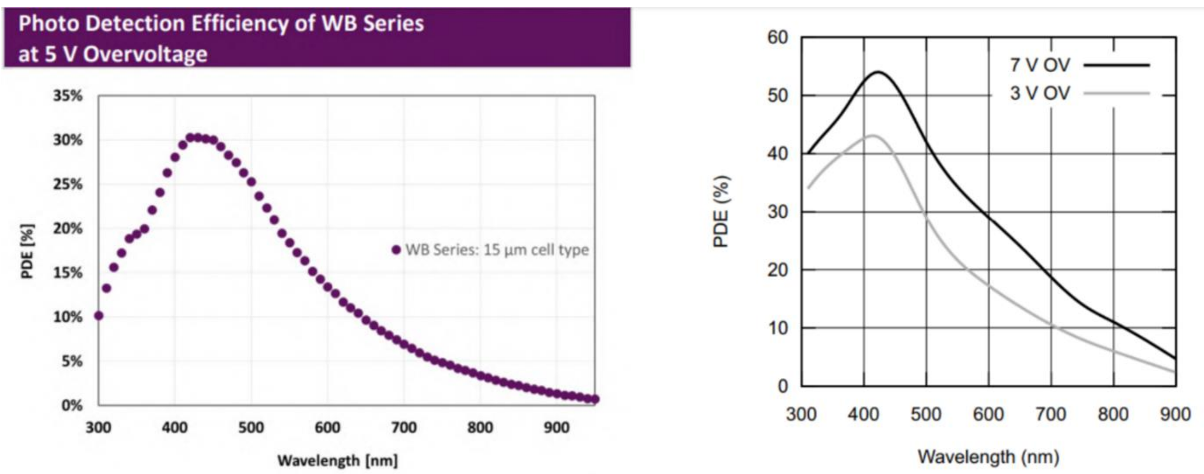

a) b)

Figure 9. The PDE as a function of wavelength for a) Ketek SiPM [8] and b) Broadcom SiPM [9].

In this project we are provided with six SiPMs: one of Ketek type, labelled SiPM 1, and five of Broadcom type, labelled SiPMs 2-6. Each SiPM sensor is mounted on a board that generates a signal, shown on figure 11, and then soldered with coloured cables. The cables that were originally soldered to the boards were too short for our setup, so we soldered new cables of length 3.5 m (figure 10).

Figure 10. Picture of the SiPM board soldered with the 3.5 m coloured cables.

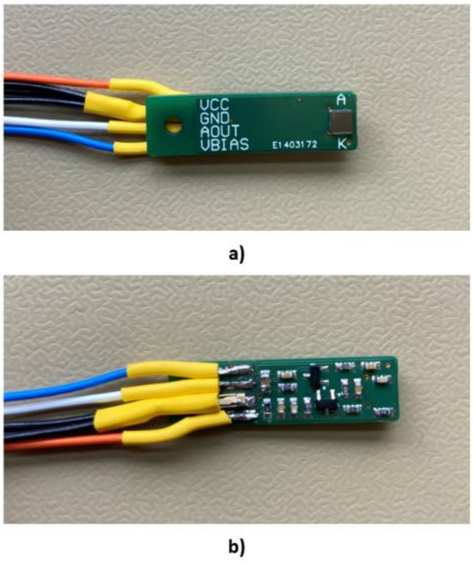

Figure 11. a) Picture of the back of the board, where the sensor is soldered. b) Picture of the front of the board, where the cables are soldered.

2.3. Overview of the experimental setup

For the purpose of measuring the efficiency of the RPC we will use two scintillators, one above and one below the RPC. In order to investigate the efficiency of the scintillators we will use the metallic trigger frame trolley shown on figure 12. The three scintillators are placed inside the three trays, which have a lid that can be removed and sealed back with screws. This allows the scintillators to be shielded from external light by the metal. The height of the trays can be adjusted using the screws in the column.

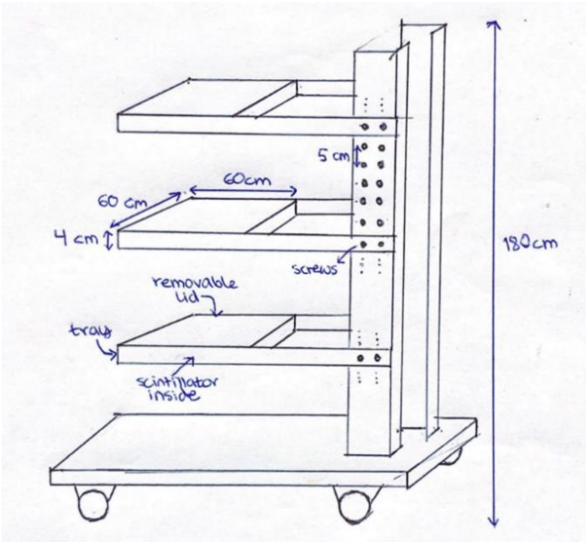

Figure 12. A sketch (drawn by me) of the trigger frame trolley used to measure the efficiency of the scintillators and RPC.

There is one SiPM placed in each of two adjacent corners in each scintillator, as shown on figure 13. It was determined that this position gave the largest efficiency, as the SiPMs cover a larger solid angle [10]. There is a cut in each corner that allows to position the SiPMs, which are then hold into place by some black tape.

Figure 13. Picture showing how the scintillator is placed inside the metal tray, with two SiPMs in the corners. A hole on the tray allows to pass through the cables of the SiPM.

To transform the signal obtained by the SiPMs into a digital signal, we use a coincidence setup (figure 14). It has four channels A, B, C and D, where the input signal (white cable) of the SiPMs is connected. There are two boards that provide a bias voltage of around 32 V to the SiPM (blue cable), which creates the high electric field. A power supply provides 6 V to the SiPM (orange cable), which is needed for its operation. If two SiPMs record a hit within a time window of 50 ns, the event is considered a coincidence. This time window is internal to the coincidence board and cannot be changed by us. The coincidence setup is connected to a computer, where a program called "tbtrigger" allows to:

1) Read the count recorded by the SiPM in each of the four channels.
2) Vary the threshold voltage for each SiPM.
3) Choose what coincidences between different SiPMs we want to record (up to 6).

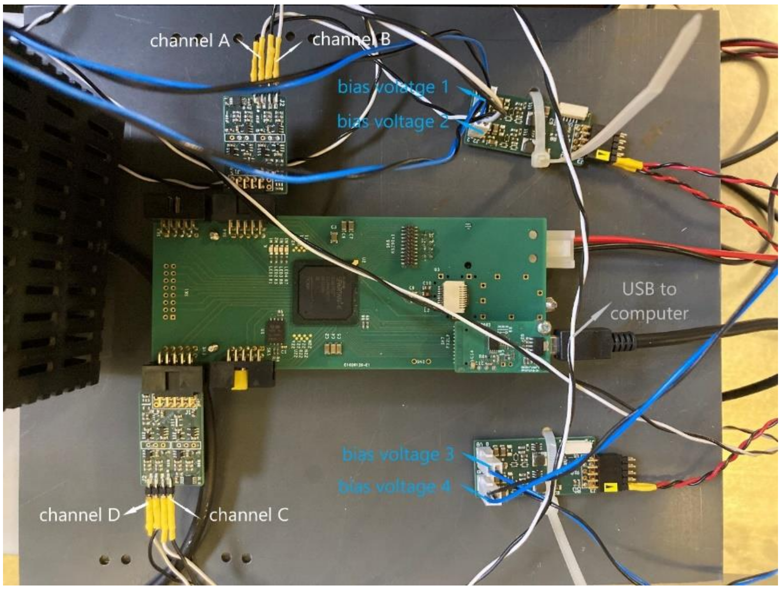

Figure 14. Picture of the coincidence setup. The channels and the bias voltage connections are marked. It is mounted on a plastic plate to isolate it from the metallic structure.

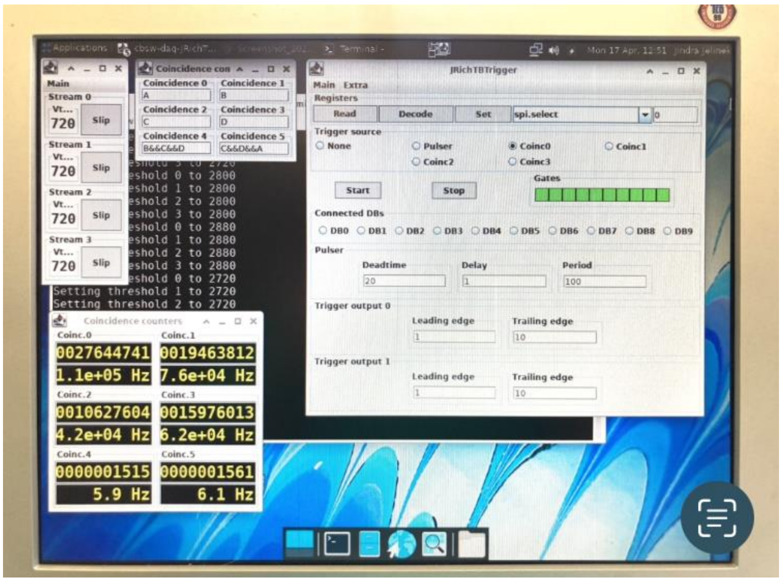

Figure 15. A screenshot of the 'tbtrigger' program in the computer, with the adjustable threshold voltage window, the coincidence configuration window and the coincidence counters.

3. Study of the efficiency of the scintillators

3.1. Checking the behaviour of the SiPMs in the oscilloscope

The first check was to test the DCR of the SiPMs. By putting each SiPM inside a black plastic bag to isolate it from external light, we made sure that we were only recording the DCR. The SiPMs were powered and connected to a digital oscilloscope. An example of the behaviour observed in the oscilloscope is given in figure 16.

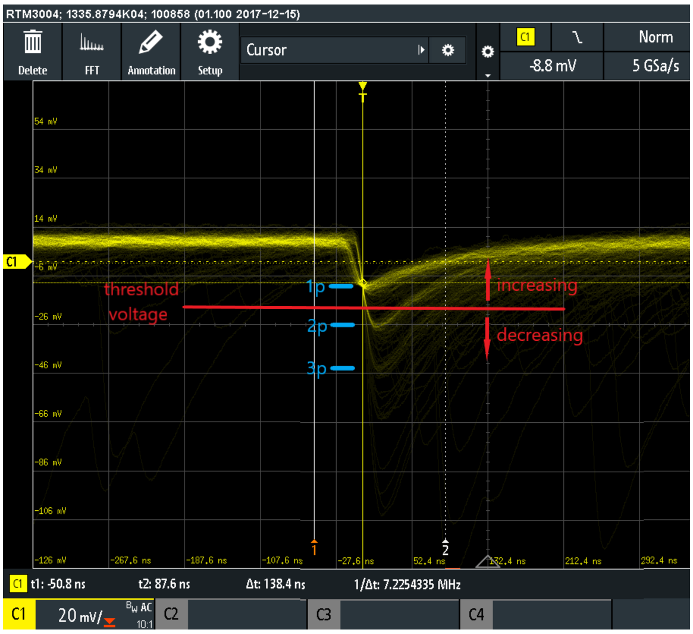

Figure 16. Screenshot of the oscilloscope signal for one of the SiPMs. The bands corresponding to one, two and three photoelectrons are marked in blue. The threshold voltage (explained in the following section) is marked in red.

We can distinguish the multiple photon bands such as those in figure 8 b), hence we can say the SiPMs are correctly detecting the thermally produced electron-hole pairs.

3.2. Variation of the rate of count with threshold voltage

Only the counts corresponding to the signals below the threshold voltage, as marked on figure 16, contribute to the recorded count. For each SiPM (still inside the black plastic bag) the rate of counts was measured for different threshold voltages. The results for SiPMs 1 and 2 are shown in figure 17.

The fractional error for a rate of counts r is:

$$\frac{\Delta r}{r} = \left(\left(\frac{\Delta t}{t} \right)^2 + \left(\frac{1}{\sqrt{N}} \right)^2 \right)^{1/2}$$

where N is the number of counts in a time t, measured with a stopwatch ($\Delta t \sim 0.5s$).

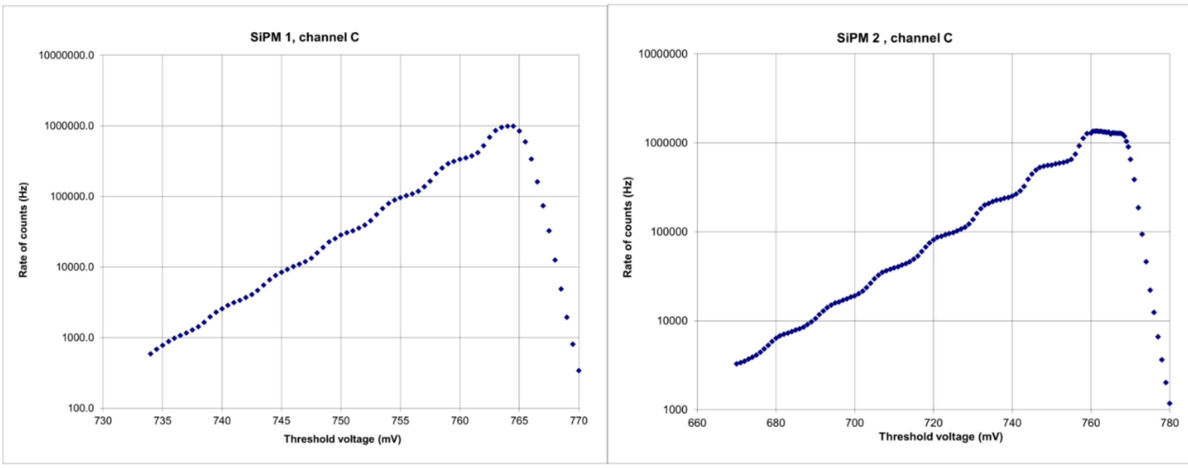

a) **b)**

Figure 17. Graphs of rate of counts against threshold voltage for a) SiPM 1(Ketek) and b) SiPM 2 (Broadcom), both connected to channel C. Errors are too small to be observed.

As the threshold voltage is decreased towards ~764mV we start to pick up the noise and the 1 photon signals. The peak corresponds to position 1 p, as labelled in figure 16. As we go past the 1 p position the count drops down, then flattens off when we start picking up the 2 photon signals. Again, the count drops down when we go over the position 2 p and then flattens off when we start picking up the 3 photon signals. And so on. As the photon density gets smaller for higher number of photon signals, the graph smears out at lower voltages. Note the difference in the shape of the peak for Ketek and Broadcom SiPMs. The graph is logarithmic; hence we can conclude that the drop in thermal noise is exponential.

We then measured the rate of counts for SiPMs 3, 4, 5 and 6 around the peak, connecting each SiPM individually to channel D. Although the position of the peak is at the same threshold voltage for all SiPMs, the height of the peak is slightly different, probably due to some individual differences between the SiPMs.

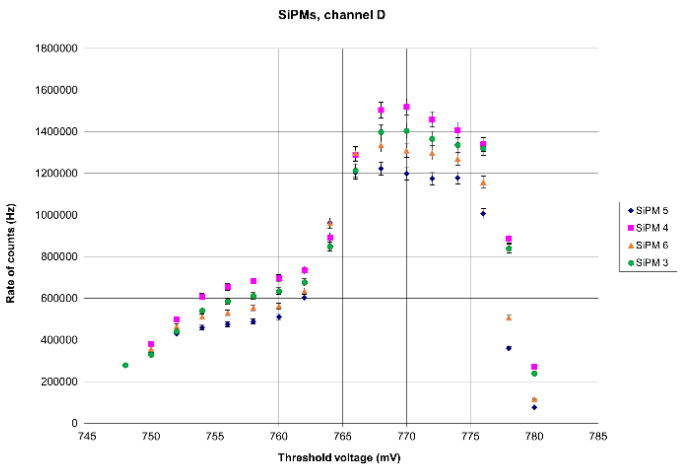

Figure 18. Graph of rate of counts against threshold voltage for SiPMs 3, 4, 5 and 6. All connected to channel D.

3.3. Variation of the rate of count with bias voltage

There is a board, shown on figure 19, that allows to adjust the bias voltage by rotating the screw. By keeping each SiPM connected to the same channel and with a fixed threshold voltage, the rate of counts was measured for each bias voltage value.

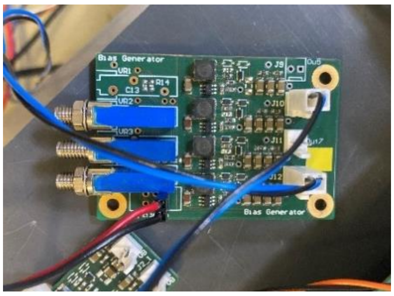

Figure 19. Picture of the board that allows to adjust the bias voltage.

In figure 20, we compare the bias voltages of SiPMs 1 and 4. The results show the same behaviour as that in figure 8 a), assuming that the rate of counts is proportional to current.

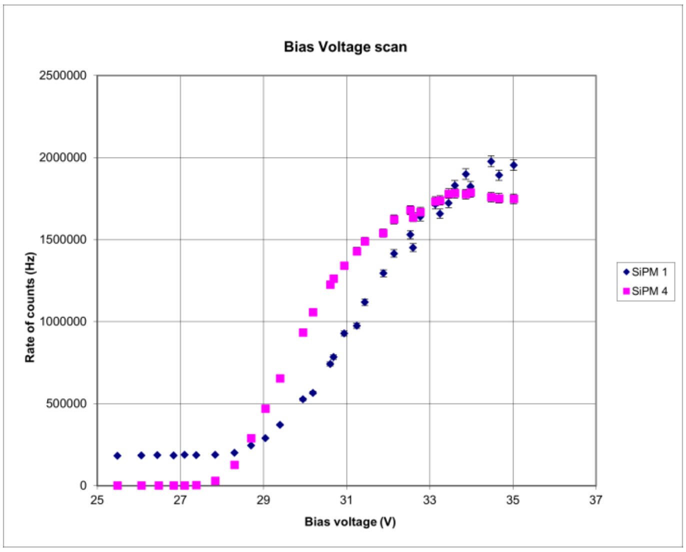

Figure 20. Graph of rate of counts against bias voltage for SiPMs 1 and 4.

SiPMs 2, 3, 5 and 6 (all Broadcom) show the same behaviour as SiPM 4, with the breakdown voltage at ~28 V. SiPM 1 has a slightly higher breakdown voltage at ~29 V. As specified in [8] and [9], the bias voltage cannot be increased further than +6 V from the breakdown voltage, where there starts to be more noise fluctuations.

It is therefore necessary to choose a bias voltage between 28/29 V and 34/35 V for the Broadcom/Ketek SiPMs. We decided that a bias voltage around 32V is a good choice.

3.4. The effect of different channels and different bias voltages

SiPMs 1 and 4 were connected to the left and right corners of scintillator 2, respectively. The rates of counts were measured for different combinations of channels and bias voltages around 32V. Here, we are working at threshold voltages around the DCR region, where the rate of count from muons is negligible (as will be explained later).

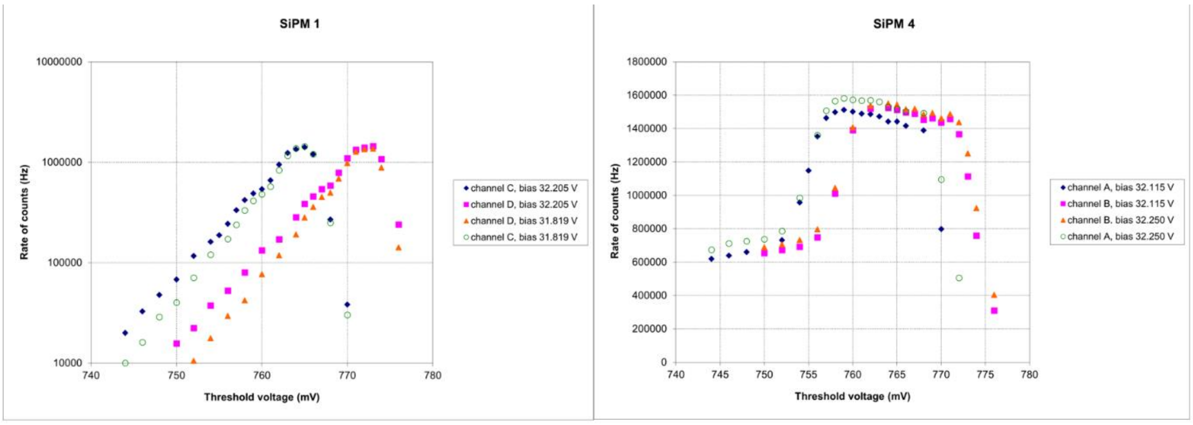

a) b)

Figure 21. Graphs of rate of count against threshold voltage for different channels and bias voltage combinations for a) SiPM 1 and b) SiPM 4.

It can be observed that at higher bias voltage the peak is slightly higher and the drop in the count rate is slower, while the position of the peak remains fixed at the same threshold voltage. Changing the channel shifts the position of the peak and also shifts slightly the height of the peak. This must be due to some offsets in the electronics of each channel.

A further study of SiPM 4 in all the four channels is shown on figure 22. It seems like the counts are different for measurements taken in different days (date indicated in figure), which could be due to changes in temperature or light intensity. Comparing the shift of the peaks between the channels in different figures, we can see that they are the same: around 8 mV between channels C-D and around 5 mV between channels A-B. Hence it can be concluded that the shift of the peak is fixed for each channel.

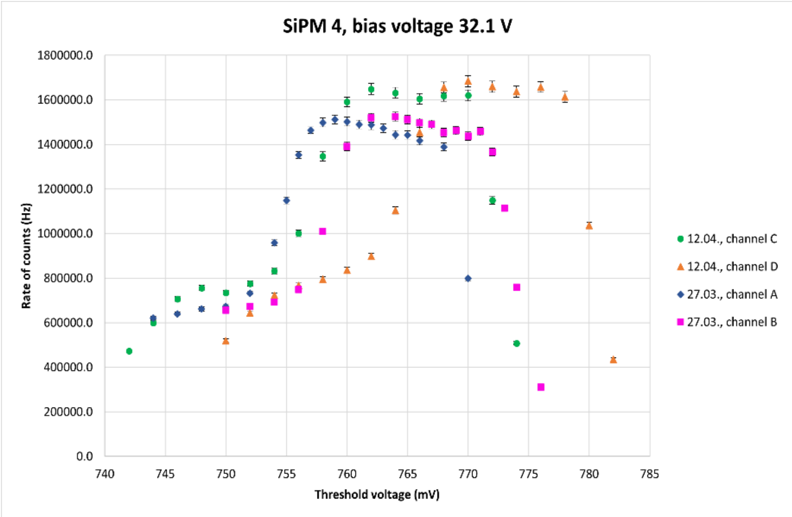

Figure 22. Count rate against threshold voltage for SiPM 4 connected to the four different channels. The date in which the measurements were taken is shown on the legend.

3.5. Coincidences in one scintillator

We placed SiPMs 3 and 4 in the left and right corners of scintillator 1, respectively. SiPM 3 was connected to channel C and SiPM 4 to channel D. We varied the threshold voltage of both SiPMs, so that their values were the same at all times, and measured for coincidences between them (for a few minutes).

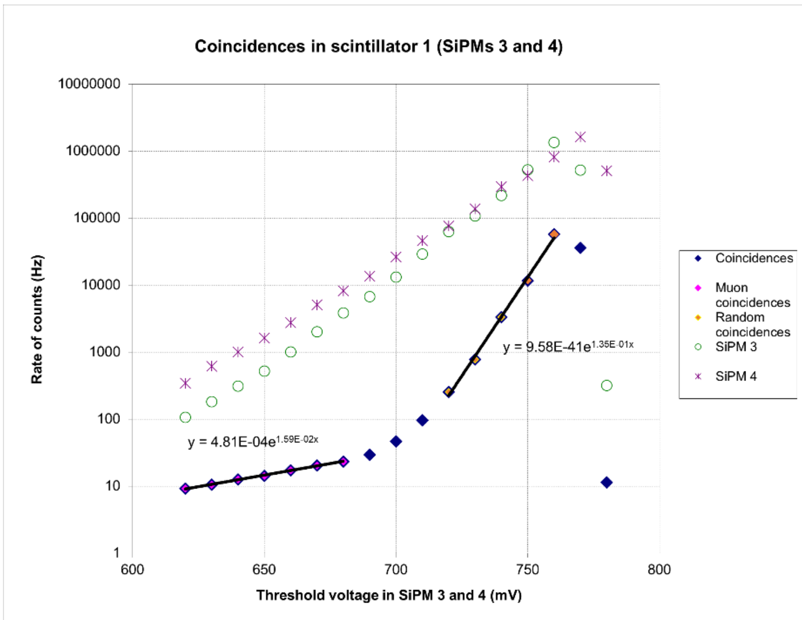

Figure 23. Graph of rate of counts against threshold voltage for SiPMs 3 and 4 and for coincidences between them.

Here, there are two types of coincidences: ones are coincidences due to the actual cosmic muons passing through the scintillator and the others are random coincidences due to the DCR in each SiPM.

In figure 23, we can distinguish the two coincidence regions. At threshold voltages below 670 mV we can say most of the coincidences are from muons and at threshold voltages above 720 mV we can say most of the coincidences are from the DCR. Using the exponential equations fitted into the lines we can determine the ratio of random coincidences to muon coincidences (R:M): it is about 1:34 at 680 mV and 1:42806 at 620 mV.

For the analysis of the efficiency of the scintillators in muon detection, we must work at threshold voltages where there is a balance of

1) Low R:M ratio
2) Large count rate – otherwise measurements take a very long time.

A voltage of 650-670 mV would work well.

3.6. Coincidences between two scintillators

We placed SiPMs 5 and 6 in the left and right corners of scintillator 2, respectively. SiPM 5 was connected to channel A and SiPM 6 to channel B. SiPMs 3 and 4 were connected to scintillator 1 as described in the previous section. The two scintillators were placed in the trigger frame trolley with a separation of 70 cm. Again, we varied the threshold voltage of all SiPMs, so that their values were always the same.

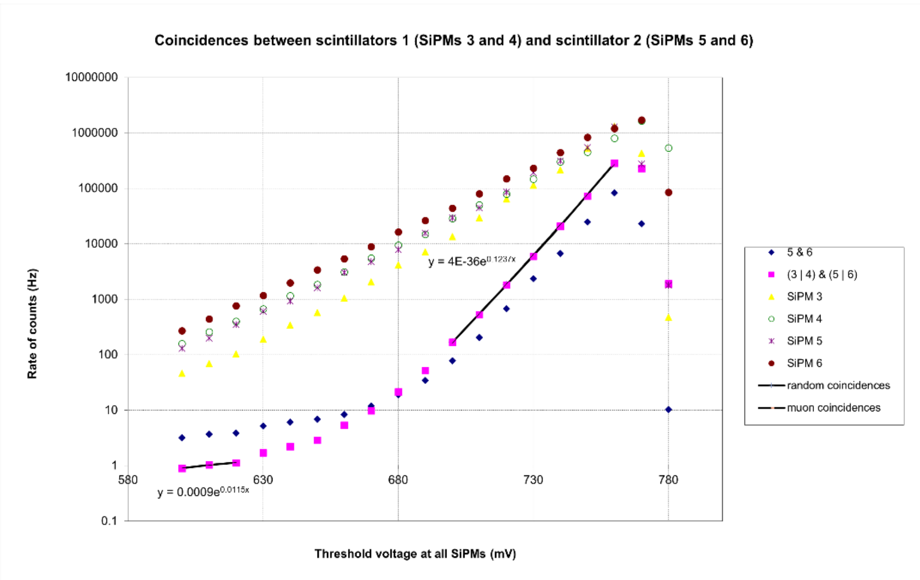

Figure 24. Graph of rate of counts against threshold voltage for SiPMs 3, 4, 5 and 6 and coincidences between them.

The coincidences between SiPMs 5 and 6 have the turning point from muon dominated region to DCR dominated region at ~700 mV, just like those for SiPMs 3 and 4 in the previous section. However, the turning point for coincidences between SiPMs (3 or 4) and (5 or 6) is at a lower threshold voltage ~670 mV. This is because there is a greater chance of random coincidences between a higher number of SiPMs and because the muons travelling at smaller angles to the horizontal only travel through one of the scintillators, hence not giving a coincidence between (3 or 4) and (5 or 6). This means there is a higher R:M ratio.

3.7. Coincidences between three scintillators – measurement of efficiency

The three scintillators were placed in the trigger frame trolley. If a muon passes through both the top and bottom scintillators, giving a coincidence, it must also pass through the middle scintillator. The efficiency of muon detection of the middle scintillator is then given by:

$$\text{Efficiency} = \frac{\text{Number of coincidences between the top, middle and bottom scintillators}}{\text{Number of coincidences between the top and bottom scintillators}}$$

The setup is described in table 1.

	Top scintillator	**Middle scintillator**		**Bottom scintillator**
	Left corner	Left corner	Right corner	Left corner
SiPM	3	5	6	4
Channel	C	A	B	D

Table 1. The configuration of the SiPMs in the top, middle and bottom scintillators, along with the channels they are connected to.

We measured for coincidences between the top and bottom scintillators (SiPMs 3 and 4) and between the top, middle and bottom scintillators (SiPMs 3 and (5 or 6) and 4).

In order to measure the efficiency of scintillator 3 we placed it in the middle position, with scintillators 1 and 2 at the bottom and top positions. The separation of the scintillators was 10 cm. First, we fixed the threshold voltage of SiPMs 3 and 4 at 650 mV, where we are certain that most of the coincidences are muons, and varied the threshold voltage of SiPMs 5 and 6. The coincidences rates were recorded for a few minutes and the efficiency was calculated. The results are shown in figure 25.

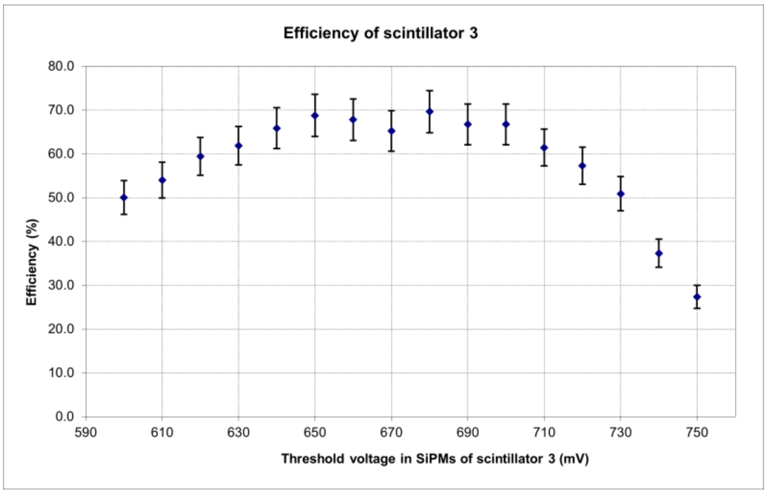

Figure 25. Graph of efficiency of scintillator 3 against the threshold voltage on its SiPMs, with the threshold voltage of the SiPMs in the top and bottom scintillators fixed at 650 mV. The dominant errors are statistical errors in the number of counts.

Up to ~680 mV, the efficiency increases as the threshold voltage increases. This is because at higher voltages the rate coincidences is larger. The R:M ratio is 1:1305 at 600 mV and 1:5 at 650 mV, hence the increase in rate is mainly due to the increase in muon coincidences. Therefore, for a given rate of counts in the top and bottom scintillators, the rate of counts in the top, middle and bottom scintillators is larger, giving a larger efficiency. After ~680 mV, the efficiency starts to drop. We believe this is due to a saturation effect, due to the large DCR at these voltages.

Another factor affecting the efficiency is the separation between the scintillators. Cosmic muons come from all directions, but only those traveling at angles closer to the vertical can pass through both three scintillators. While the height of the middle scintillator was fixed, the separation between the top and bottom scintillators was varied from 20 cm to 105 cm.

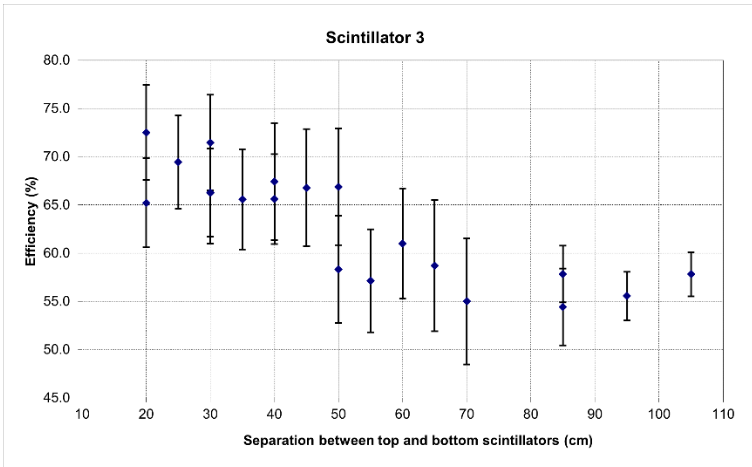

Figure 26. Graph of efficiency against separation between the top and bottom scintillators.

At closer separation, we can also pick up the muons travelling at lower angles to the horizontal. These muons travel a longer distance through the scintillators and release more photons. Both factors increase the rate of muon coincidences. Hence, for a given number of measured coincidences, the R:M ratio is lower, giving a larger efficiency.

It was important to check if the way in which the SiPMs are attached to the corners of the scintillators affected their PDE and the overall efficiency of the scintillator. To do this, we removed SiPMs 5 and 6, then placed them again into the same position and took the coincidence measurements. The procedure was repeated 6 times.

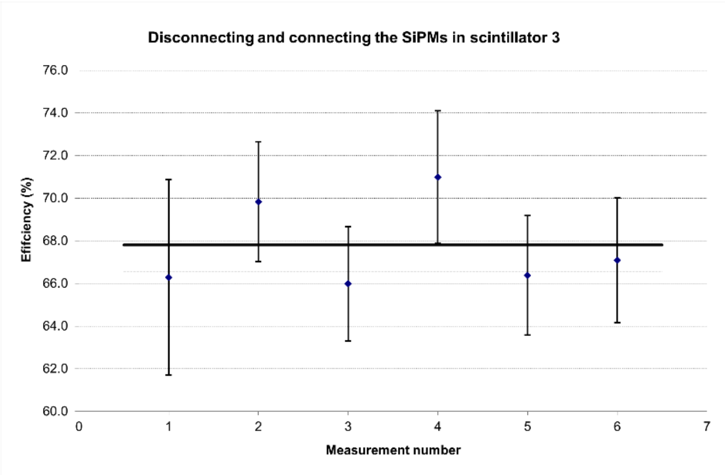

Figure 27. Graph showing the effect of disconnecting and connecting the SiPMs in scintillator 3. The threshold voltages were fixed at 650mV for SiPMs 3 and 4, and at 670mV for SiPMs 5 and 6. The separation between the scintillators was 10cm.

All the variations in efficiency are within statistical error. Hence it can be concluded that the way in which the SiPMs are attached into the scintillators does not affect the efficiency.

The detailed measurements of the efficiencies of scintillators 1 and 2 are given in the appendices.

In Figure 28 we compare the efficiency curves for the three scintillators.

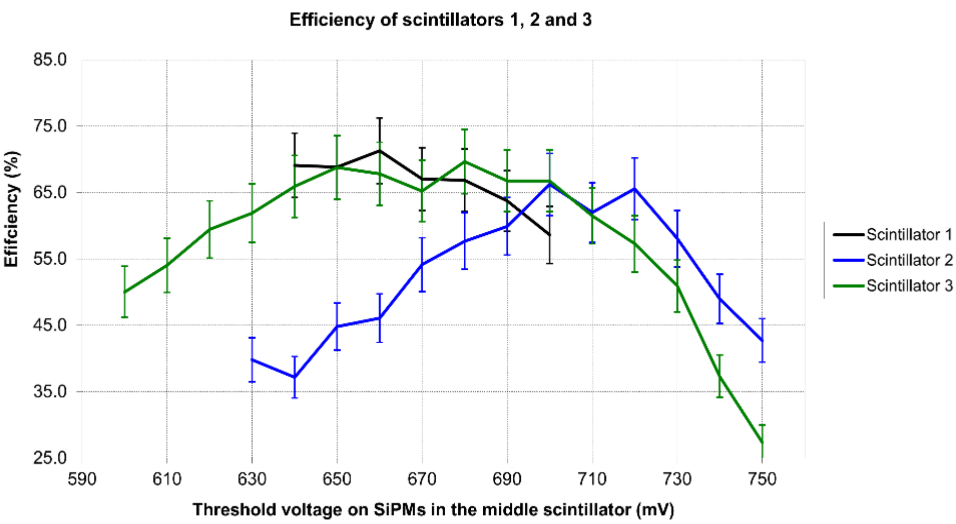

Figure 28. Graph of efficiency against threshold voltage for scintillators 1, 2 and 3. The separation was 10 cm for all three scintillators.

	Scintillator 1	Scintillator 2	Scintillator 3
Peak efficiency (%)	71.3	66.2	69.6
Peak threshold voltage (mV)	660	700	680

Table 2. Shows the peak efficiency and threshold voltage of each scintillator.

Each scintillator seems to have a different efficiency, with scintillator 2 having the lowest of all 3. We believe this is due to individual differences in the scintillator themselves, such as some internal cracks. It would then be ideal to use scintillators 1 and 3 to take the efficiency measurements of the RPC.

3.8. Damaged SiPMs and new SiPMs

After doing some further experiments swapping the positions of the SiPMs, we suddenly observed that SiPMs 2, 3 and 5 were giving very low counts. They didn't show the usual behaviour in the oscilloscope and when they were then inspected under the microscope some cracks and broken corners were observed.

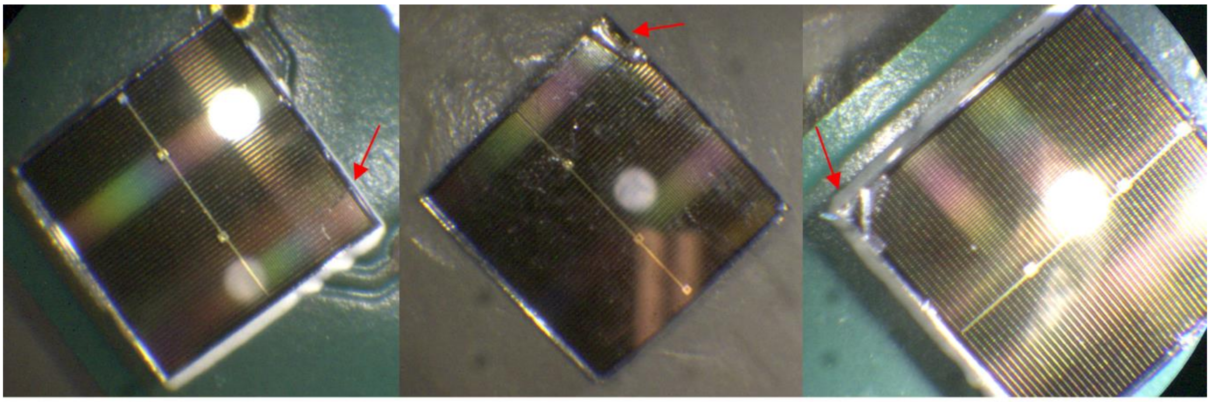

a) b) c)

Figure 29. Pictures of the three damaged SiPMs. The cracks are marked by a red arrow.

It was strange that these three SiPMs were mechanically damaged at the same time. It was perhaps in the process of removing and placing them back in the corners of the scintillators. The SiPMs were tightly taped into the corners, which could have applied a lot of pressure and cracked the sensors.

The damaged SiPM sensors were removed from the board by Dr Stephen Wotton and new sensors (of Broadcom type) were soldered into the same boards. This new SiPMs were labelled SiPMs 7, 8 and 9. I soldered new cables of thinner diameter in order to allow easier handling of the SiPMs. They were observed in the oscilloscope and showed the correct behaviour with the multiple photon bands. The oscilloscope screenshot for SiPM 8 is given in figure 30 as an example.

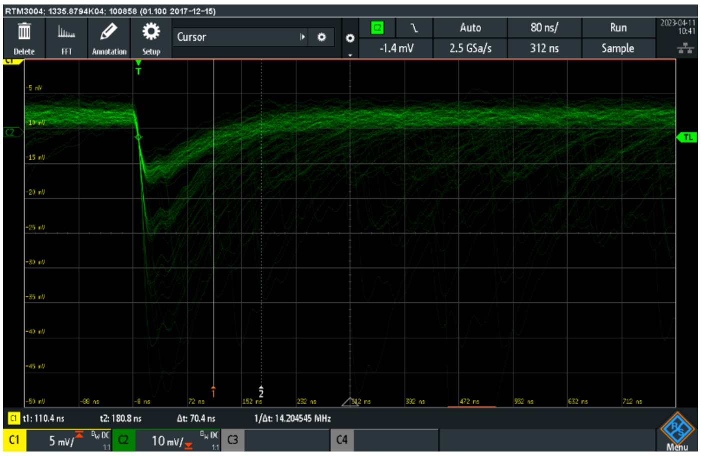

Figure 30. Oscilloscope screenshot for SiPM 8.

4. Study of the efficiency of the RPC

4.1. Testing the free front-end boards

There are 4 FEBs which are not soldered to the RCP, referred here as 'free FEBs': 209E, 216E, 201E and 82E. 209E is missing a black piece (protective cover for the chip), 216E and 201E are missing some capacitors and 82E is not missing any piece.

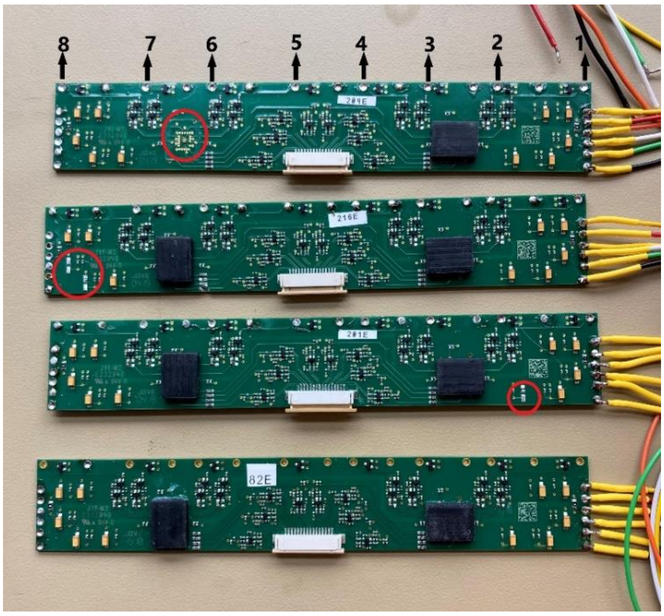

Figure 31. Picture of FEBs 209E, 216E, 201E and 82E. The missing pieces are circled in red. The output connections 1-8 are marked with black arrows.

Each FEB was soldered with 6 coloured wires connected to low voltage power supplies as specified in table 3.

Cable	Code	Applied voltage (V)
Black	GND	-
Green	V_LVDS	2.50
White	V_DISC	2.60
Orange	V_PU	0.30
Red	V_AMP	1.30
Yellow	V_th_LV1	1.80

Table 3. The required voltages for each coloured cable in the front-end boards.

The FEB is then connected to an oscilloscope by the output ribbon cable connector. A probe from the oscilloscope is connected to one pair of pins on the end of the ribbon cable, each pin corresponding to one of the eight output connections. The connections were touched with the finger one at a time, while being grounded by an EDS bracelet, in order to induce a signal. The responses for each FEB are presented in table 4.

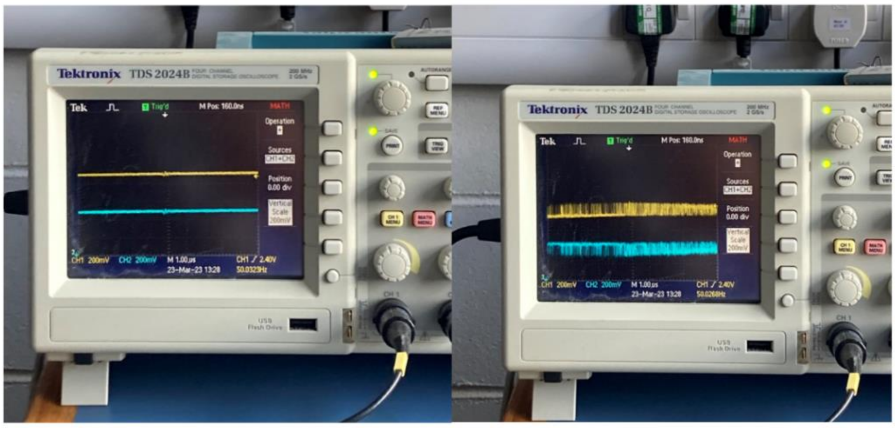

a) b)

Figure 32. a) Picture of the oscilloscope screen when the connection is not touched, showing no signal. b) Picture of the oscilloscope screen when the connection is touched, showing an induced signal.

FEB	Output 1	Output 2	Output 3	Output 4	Output 5	Output 6	Output 7	Output 8
209E	✓	✓	✓	✓	×	×	✓	×
216E	✓	✓	✓	✓	✓	×	×	×
201E	✓	✓	✓	✓	✓	✓	✓	✓
82E	✓	✓	✓	✓	✓	✓	✓	✓

Table 4. Responses of the FEBs when the connection outputs are touched by the finger. The symbol ✓ means a signal is observed and the symbol × means a signal is not observed.

4.2. Testing the front-end boards attached to the RPC

Six coloured wires were soldered to the leftmost FEB in the eta side and to the leftmost FEB in the phi side, and they were connected to the relevant low voltage power supplies running with the same voltages as specified in table 3. Each FEB was tested in turn by connecting it to the oscilloscope and touching the connections with the finger, while grounded. However, no induced signal was observed in the oscilloscope. Three FEBs in the eta side and four FEBs in the phi side were tested, but none showed any signal. To check whether the problem was with the setup circuit or with the actual FEBs, I connected one of the free FEBs to the same setup and it did show a signal under the oscilloscope.

It was important to check if any of the FEBs was consuming a large amount of current. I used a board built with 100 mΩ resistors, shown in figure 33, to measure the voltage across each cable, which gives a measure of the current. I measured the current through FEB 82E and through the eta side and phi side, for which we expect the current to be increased by a factor of four and eight, respectively.

	Free FEB		Eta side			Phi side	
Cable	Voltage (mV)	Current (mA)	Voltage (mV)	Current (mA)	Current (short fixed) (mA)	Voltage (mV)	Current (mA)
Yellow	0.41	4.10	1.60	16.0	16.4	3.15	31.5
Red	0.87	8.70	80.0	800	36.0	7.23	72.3
Orange	0.00	0.00	0.00	0.00	0.00	0.00	0.00
White	4.07	40.7	15.96	159.6	160.6	30.60	306.0
Green	6.15	61.5	23.88	238.8	240.3	46.44	464.4

Table 5. The measured voltages and their corresponding currents for each coloured cable.

An anomalously high current was observed in the red cable in the eta side. With the help of a technician, I did some voltage tests and found out there was a short in one of the FEBs. After it was fixed, the FEBs in the eta side were tested again but no signal was observed.

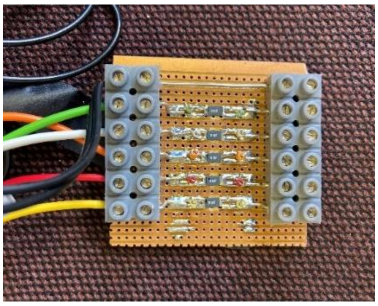

Figure 33. Picture of the board used to measure the currents through the FEBs.

The technician removed one of the FEBs in the eta side. I tested it under the oscilloscope, and it did show a signal for each of the eight connections when touched. We believe that the reason why the FEBs are not responsive when soldered into the RPC is because the RPC strips have a very high capacitance, and the discharge generated by touching the connections is not large enough to generate a signal that can be seen in the oscilloscope.

The last step was to connect the RPC to the Data Acquisition system (DAQ), shown on figure 34, which reads out events recorded by the FEBs. A program in the computer connected to the DAQ allows to read the digitalised events. First, the DAQ was tested by using hits simulated by a function generator. Then, the FEBs in the eta side were connected by output ribbon cables to a main ribbon cable carrying the signal from the 32 strips, as shown in figure 35, and connected to the DAQ. When the low voltage system was off, a large number of events was observed. This is because with the V_LVDS voltage off, the operation of the TDCs (Time-to-Digital Converters) does not function correctly. When the low voltage system was turned on, very few events were observed, which correspond to noise signals. A high voltage must be applied to the RPC in order to observe cosmic muon events.

Figure 34. Picture showing the DAQ. The function generator and the ribbon cable from the RPC are marked in blue.

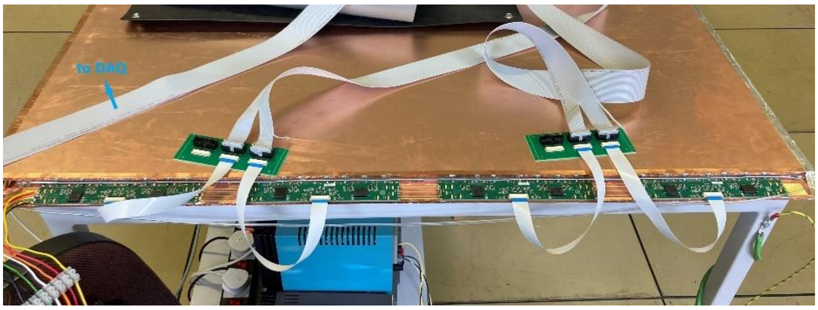

Figure 35. Picture showing the FEBs in the eta side connected by the output ribbon cables.

Conclusion

Throughout this project we completed some of the necessary steps required to reach the goal of measuring the efficiency of the RPC singlet using different gases.

First, we confirmed the behaviour of the SiPMs with an oscilloscope and investigated the dark count rate at different threshold voltages and bias voltages. The peak was found to be at 765 ± 10 mV, depending on which channel the SiPM was connected to. We found the breakdown voltages are at 28/29 V for the Ketek/Broadcom type SiPMs and decided to use a bias voltage around 32 V to give a sufficiently large rate of counts.

The coincidences between SiPMs in two scintillators were measured. It was found that at threshold voltages below 680 mV the majority of coincidences were due to cosmic muons and above 680 mV the majority were random coincidences due to the DCR in each SiPM. We decided to work at threshold voltages around 650-680 mV in order to have a low R:M ratio, but also obtain a rate of counts large enough to allow the measurements to be taken in a reasonable amount of time.

A setup with three scintillators was used to determine the efficiency of the middle scintillator. The maximum efficiencies for scintillators 1, 2 and 3 were found to be 71.3%, 66.2% and 69.6% at threshold voltages of 660, 700 and 680 mV respectively. Also, the efficiency was found to be larger when the separation between the scintillators was smaller.

It would be interesting to see the effect of the coincidence time window on the rate of random coincidences. Increasing the time window would theoretically decrease the rate of random coincidences but keep the rate of muon coincidences unchanged, given that this time window is still larger than the time taken for the muons to travel between the scintillators.

To measure the efficiency of the RPC singlet in future studies, the proposal is to use a setup with two scintillator detectors, ideally scintillators 1 and 3, positioned above and below the RPC. The separation between scintillators 1 and 3 must be 20 cm and the threshold voltages of their SiPMs must be 660 and 680 mV, respectively.

The FEBs soldered to the ends of the strips in the eta and phi sides of the RPC were powered with low voltage supplies and were tested by inducing a signal with the finger to the connection outputs. Although no response was observed for any of the soldered FEBs, they did give a response when they were removed from the RPC, which suggests they are working. The large capacitance of the RPC strips is likely the reason why the signal induced by the finger is not enough to be observed under the oscilloscope.

Finally, the FEBs in the eta side of the RPC were connected to the DAQ and a first few operation tests were carried out to study the detection of noise. We confirmed that when the low voltage system was turned off, the operation of the TDCs does not function correctly and a lot of noise is recorded. In future studies, the RPC should be powered with a high voltage system to start recording hits from cosmic muons.

These studies aim to help with the commissioning of the current proANUBIS prototype installed in the ATLAS cavern and with the upcoming proANUBIS prototype that will provide future performance studies using eco gases in the RPCs.

It might be that ANUBIS is on the way to finding new LLPs that could revolutionise our current understanding of particle physics.

5. Appendices

5.1. Appendix A: Efficiency of scintillators 1 and 2.

Here, we used the same method as that described in section 3.7 to find the efficiency of scintillators 1 and 2.

We placed scintillator 2 in the middle position, with scintillators 1 and 3 at the top and bottom positions. With a separation of 10 cm between the scintillators and the threshold voltage of the SiPMs in the top and bottom scintillators fixed at 650 mV. The graph of the efficiency against threshold voltage of the SiPMs in scintillator 2, figure 36, shows the same behaviour as scintillator 3.

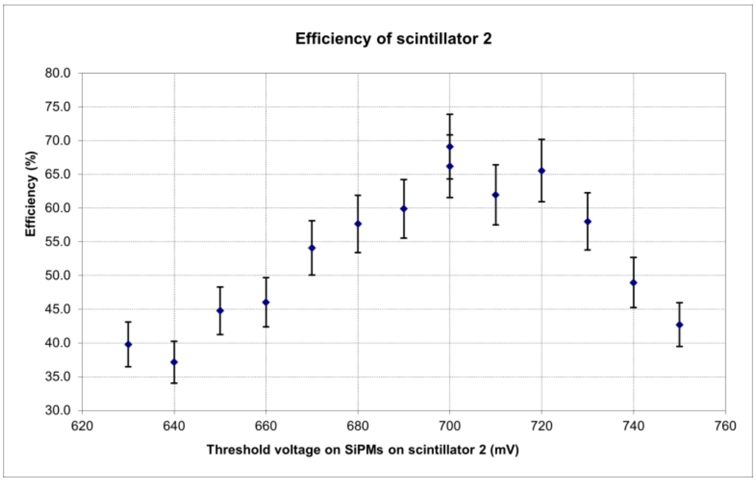

Figure 36. Graph of efficiency of scintillator 2 against the threshold voltage on its SiPMs, with the threshold voltage of the SiPMs in the top and bottom scintillators fixed at 650 mV.

Then we fixed the voltages of the SiPMs in scintillator 2 to 670mV and varied the voltages of the SiPMs in the top and bottom scintillators. This was done at two different separations: 35 cm and 10 cm.

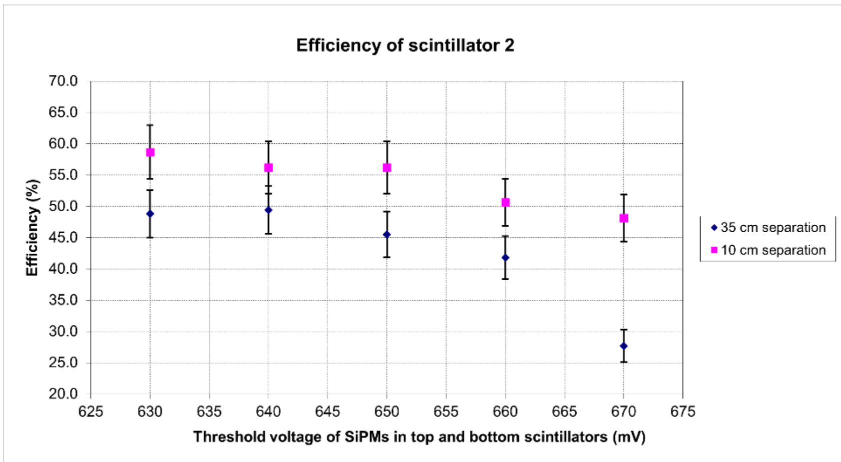

Figure 37. Graph of the efficiency of scintillator 2 against the threshold voltage in the SiPMs in the top and bottom scintillators, with the threshold voltage of the SiPMs in scintillator 2 fixed at 670 mV. Measurements taken at separations 10 cm and 35 cm.

The efficiency decreased as the voltage was increased. This is because for a given number of coincidences between the SiPMs in the top and bottom scintillators, at higher threshold voltages there is a higher fraction of random coincidences which have less chance of giving a coincidence with the SiPMs in the middle scintillator, hence giving a smaller efficiency. As expected, the efficiencies are larger at a separation of 10 cm.

Then we placed scintillator 1in the middle position, with scintillators 2 and 3 at the top position and bottom positions. Again, the separation was set to 10 cm between the scintillators and the threshold voltage of the SiPMs in the top and bottom scintillators was fixed at 650 mV. To test the effect of swapping the positions of the SiPMs within a scintillator, the measurements were also taken with SiPMs 5 and 6 swapped.

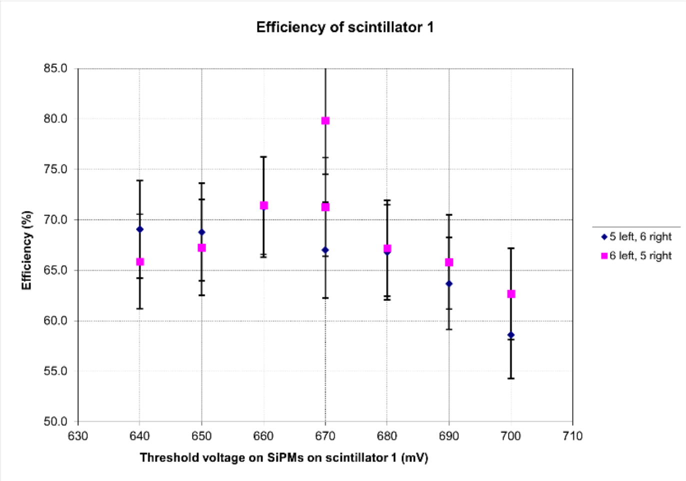

Figure 38. Graph of efficiency of scintillator 1 against threshold voltage of its SiPMs, with the threshold voltage of the SiPMs in the top and bottom scintillators.

Figure 36 shows that swapping the SiPMs within a scintillator has no significant effect on the efficiency, as all variations are within error.

We then fixed the voltages of the SiPMs in scintillator 1 to 670mV and varied the voltages of the SiPMs in the top and bottom scintillators, with a separation of 10 cm. The results show the same behaviour as scintillator 2.

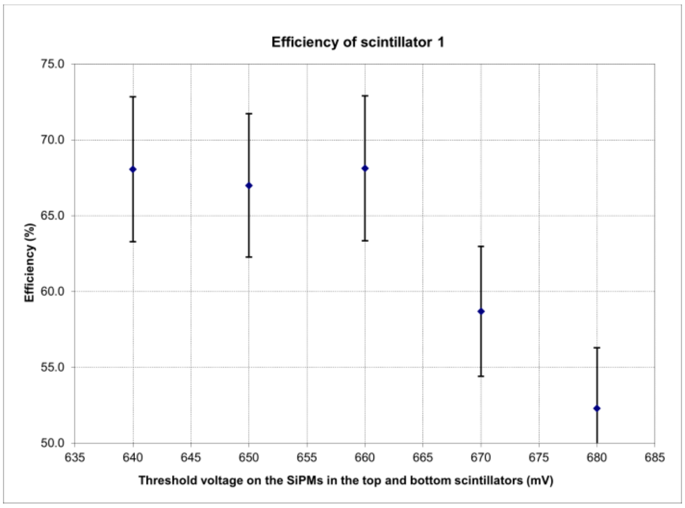

Figure 39. Graph of the efficiency of scintillator 1 against the threshold voltage in the SiPMs in the top and bottom scintillators, with the threshold voltage of the SiPMs in scintillator 2 fixed at 670 mV.

5.2. Appendix B: Cosmic muons

When a high energy primary particle coming from space collides with a nucleus of the upper atmosphere, it generates a spray of particles. Among these secondary particles are short lived pions that decay into muons and muon neutrinos.

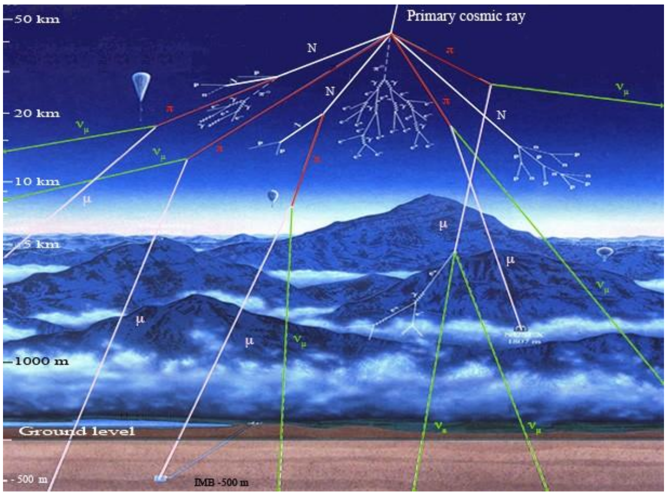

Figure 40. Picture showing the interaction of cosmic rays in the atmosphere and the production of muons [11].

The average lifetime of a muon is 2.2 µs, which might seem very short, but is sufficient to allow muons to travel long distances in the atmosphere and reach the ground level. Indeed, most of the cosmic muons have a high energy and travel at speeds close to 300 000 km/s, the speed of light in vacuum.

Muons arrive at the ground level at different angles from the zenith. The average muon flux distribution can be approximated to first order as a function of $\cos^2(\theta)$, where θ is the angular displacement from the zenith. This distribution should vary depending on the energy ranges that are being considered. At higher energies the distribution is flattened, and at low energies the distribution is steeper.

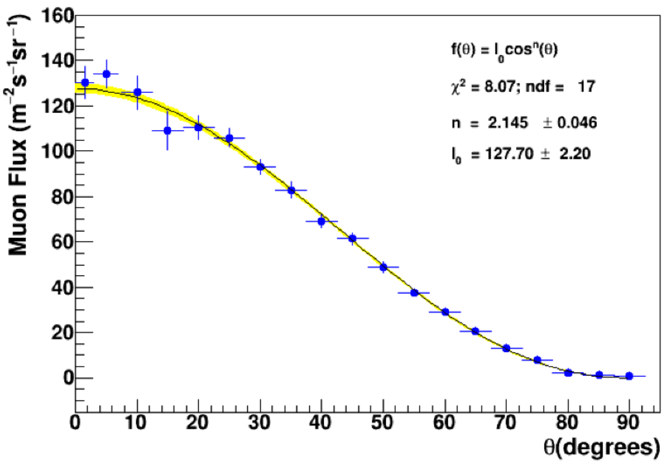

Figure 41. Graph of the muon flux against the angle from the zenith [12].

During its journey, the muon has little chance to interact. Being 207 times heavier than electrons, it is much less subject to the Bremsstrahlung effect, which is the main source of deceleration for electrons and positrons of similar energy. This makes muons very penetrating.

At sea level, the flow of muons is about 170 muons m^{-2} s^{-1}.

Glossary

ANUBIS AN Underground Belayed In-Shaft search experiment

ATLAS A Toroidal LHC ApparatuS

BSM Beyond Standard Model

CMS Compact Muon Solenoid

DAQ Data Acquistion system

DCR Dark Count Rate

FEB Front-End Board

LHC Large Hadron Collider

LHCb Large Hadron Collider beauty

LLP Long-Lived Particle

PDE Photon Detection Efficiency

SiPM Silicon Photomultiplier

SM Standard Model

SUSY Supersymetry

TDC Time-to-Digital Converter

R:M Random coincidences: Muon coincidences

RPC Resistive Plate Chamber

References

[1]. Chou, J. P., Curtin, D., & Lubatti, H. (2017). New detectors to explore the lifetime frontier. Physics Letters B, 767, 29–36. 3.

[2]. Gligorov, V. V., Knapen, S., Papucci, M., & Robinson, D. J. (2018). Searching for long-lived particles: A compact detector for exotics at LHCb. Phys. Rev. D, 97, 015023.

[3]. Bauer, M., Brandt, O., Lee, L., & Ohm, C. (2019). ANUBIS: Proposal to search for long lived neutral particles in CERN service shafts.

[4]. Peabody, S.T. (2022). Sensitivity of the ANUBIS and ATLAS Detectors to Neutral Long-Lived Particles Produced in pp Collisions at the Large Hadron Collider. University of Cambridge, Cambridge.

[5]. Français, V. (2017). Description and simulation of the physics of Resistive Plate Chambers. Laboratoire de Physique Corpusculaire - Clermont-Ferrand.

[6]. ELJEN TECHNOLOGY. General Purpose Plastic Scintillator EJ-200, EJ-204, EJ-208, EJ-212 (2021). https://eljentechnology.com/products/plastic-scintillators/ ej-200-ej-204-ej-208-ej-212

[7]. sensL. An Introduction to the Silicon Photomultiplier, (2017). https://cernbox.cern.ch/index.php/s/1NSCluoAatGCMZu.

[8]. Ketek. Product Data Sheet SiPM Silicon Photomultiplier PM3315-WBB0, Rev. 12/2018. https://www.ketek.net/wp-content/uploads/2018/12/ KETEK-PM3315-WB-B0-Datasheet.pdf.

[9] Broadcomő. AFBR-S4N33C013 NUV-HD Single Silicon Photo Multiplier (2022). https://docs.broadcom.com/doc/AFBR-S4N33C013-DS.

[10]. Reymermier, T. (2022). Timing coincidence trigger setup. Cavendish Laboratory, University of Cambridge.

[11]. Radioactivity.eu.com Muons in the atmosphere, a component of cosmic rays https://radioactivity.eu.com/in_daily_life/cosmic_muons

[12]. Borja, C., Avila, C., Roque, G., and Sanchez, M. (2022). Atmospheric Muon Flux Measurement near Earth's Equatorial Line. Universidad de los Andes, Bogota.